

Magnetic fields in galactic environments probed by Fast Radio Bursts

Ilya S. Khrykin¹, Nicolas Tejos¹, J. Xavier Prochaska^{2,3,4,5}, Alexandra Mannings², Lluís Mas-Ribas², Kentaro Nagamine^{3,7,8,9,10}, Khee-Gan Lee^{3,6}, Bryan Gaensler², Zhao Joseph Zhang⁷, and Lucas Bernales-Cortés¹

¹ Instituto de Física, Pontificia Universidad Católica de Valparaíso, Casilla 4059, Valparaíso, Chile
e-mail: i.khrykin@gmail.com

² University of California, Santa Cruz, 1156 High St., Santa Cruz, CA 95064, USA

³ Kavli IPMU (WPI), UTIAS, The University of Tokyo, Kashiwa, Chiba 277-8583, Japan

⁴ Division of Science, National Astronomical Observatory of Japan, 2-21-1 Osawa, Mitaka, Tokyo 181-8588, Japan

⁵ Simons Pivot Fellow

⁶ Center for Data-Driven Discovery, Kavli IPMU (WPI), UTIAS, The University of Tokyo, Kashiwa, Chiba 277-8583, Japan

⁷ Theoretical Astrophysics, Department of Earth & Space Science, Graduate School of Science, The University of Osaka, 1-1 Machikaneyama, Toyonaka, Osaka 560-0043, Japan

⁸ Theoretical Joint Research, Forefront Research Center, Graduate School of Science, The University of Osaka, 1-1 Machikaneyama, Toyonaka, Osaka 560-0043, Japan

⁹ Department of Physics & Astronomy, University of Nevada, Las Vegas, 4505 S. Maryland Pkwy, Las Vegas, NV 89154-4002, USA

¹⁰ Nevada Center for Astrophysics, University of Nevada, Las Vegas, 4505 S. Maryland Pkwy, Las Vegas, NV 89154-4002, USA

September 12, 2025

ABSTRACT

Fast Radio Bursts (FRB) are extragalactic, bright, millisecond radio pulses emitted by yet unknown sources. FRBs constitute a unique probe of various astrophysical and cosmological environments via their characteristic dispersion (DM) and Faraday rotation (RM) measures that encode information about the ionized gas traversed by the radio waves along the FRB line-of-sight. In this work, we analyse the observed RM measured for 14 localized FRBs in the redshift range $0.05 \leq z_{\text{frb}} \leq 0.5$, in order to infer the total magnetic field, B , in various galactic environments. Additionally, we calculate f_{gas} - the average fraction of halo baryons in the ionized CGM. We build a spectroscopic dataset of FRB foreground galaxy halos, acquired with VLT/MUSE observations and by the FLIMFLAM collaboration. We develop a novel Bayesian statistical algorithm and use it to correlate the information of the individual intervening halos with the observed RM_{obs} . This approach allows us to disentangle the magnetic fields present in various environments traversed by the FRB sightlines. Our analysis yields the first direct FRB constraints on the strength of magnetic fields in the interstellar medium (ISM) ($B_{\text{host}}^{\text{local}}$) and in the halo ($B_{\text{host}}^{\text{halo}}$) of the FRB host galaxies, as well as in the halos of foreground galaxies and groups ($B_{\text{f/g}}^{\text{halo}}$). We find that the average magnetic field strength in the ISM of the FRB host galaxies is $B_{\text{host}}^{\text{local}} = 5.44^{+1.13}_{-0.87} \mu\text{G}$. Additionally, we place an upper limit on the average magnetic field strength in FRB host halos, $B_{\text{host}}^{\text{halo}} \lesssim 4.81 \mu\text{G}$ and in foreground intervening halos, $B_{\text{f/g}}^{\text{halo}} \lesssim 4.31 \mu\text{G}$. Moreover, we estimate the average fraction of cosmic baryons inside $10 \leq \log_{10}(M_{\text{halo}}/M_{\odot}) \leq 13.1$ halos to be $f_{\text{gas}} = 0.45^{+0.21}_{-0.19}$. We find that the magnetic fields strengths inferred in this work are in good agreement with previous measurements. In contrast to previous studies that analysed FRB RMs and have not considered contributions from the halos of the foreground and/or FRB host galaxies, we show that they can contribute a non-negligible amount of RM and must be taken into account when analysing future FRB samples.

Key words. Galaxies: halos – Galaxies: magnetic fields – ISM: magnetic fields

1. Introduction

Over the last decades, extragalactic millisecond radio transients termed Fast Radio Bursts (FRB; Lorimer et al. 2007), have been established as remarkable probes of physical processes spanning a vast range of scales: from atomic to cosmological (e.g. Petroff et al. 2022). While traversing through the plasma in different cosmic environments, the FRB signal experiences a dispersion caused by the free electrons along the propagation path, resulting in a frequency-dependent time delay of the arrival of photons at the telescopes on Earth. This characteristic dispersion, referred to as the dispersion measure (DM), has been used extensively to solve the so-called *missing* baryon problem (McQuinn 2014; Macquart et al. 2020) and to infer how these baryons are distributed in the intergalactic (IGM) and circumgalactic

(CGM) media (Simha et al. 2020; Khrykin et al. 2024b; Connor et al. 2025). In addition, analysis of the FRB DM provides a tool for measuring cosmological parameters (e.g., James et al. 2022; Wang et al. 2025; Glowacki & Lee 2024; Fortunato et al. 2025) as well as for assessing galaxy feedback mechanisms (e.g. Khrykin et al. 2024a; Medlock et al. 2025; Zhang et al. 2025; Guo & Lee 2025; Dong et al. 2025; Sharma et al. 2025).

Furthermore, if the propagation medium is magnetized, the intrinsic FRB polarization angle experiences a frequency-dependent rotation, characterized by the quantity dubbed the rotation measure (RM). Akin to DM, RM is proportional to the integrated number density of electrons along the propagation path, but additionally weighted by the magnetic field component parallel to the FRB sightline. It, therefore, offers an opportunity to

Table 1. Sample of 14 FRBs analysed in this work. From left to right the columns show: full FRB name in TNS standard, right ascension, declination, FRB redshift, observed dispersion and rotation measures, total contribution to the rotation measure from the Milky Way (halo and ISM), instrument or survey used to collect narrow-field spectroscopic information of foreground galaxies.

FRB ID	R.A. deg	Dec. deg	Redshift	DM _{obs} ^b pc cm ⁻³	RM _{obs} ^c rad m ⁻²	RM _{MW} ^d rad m ⁻²	Source of Narrow-field Data
FRB 20211127I ^a	199.8087	-18.8380	0.0469	234.8	-67.0 ± 1.0	-2.90 ± 6.2	2dF-AAOmega, 6dF
FRB 20211212A ^a	157.3507	+01.3605	0.0707	206.0	+21.0 ± 7.0	+6.0 ± 5.7	2dF-AAOmega
FRB 20190608B ^a	334.0199	-07.8983	0.1178	338.7	+353.0 ± 1.0	-24.4 ± 13.3	SDSS, KCWI, MUSE
FRB 20200430A ^a	229.7064	+12.3768	0.1610	380.0	-195.3 ± 0.7	+14.5 ± 7.0	LRIS, DEIMOS, MUSE
FRB 20210117A	339.9795	-16.1515	0.2145	729.2	-45.8 ± 0.7	+3.3 ± 9.2	MUSE
FRB 20191001A ^a	323.3513	-54.7477	0.2340	506.9	+51.1 ± 0.4	+23.5 ± 4.3	2dF-AAOmega, MUSE
FRB 20210320C	204.4608	-16.1227	0.2797	384.6	+288.8 ± 0.2	-2.8 ± 5.7	MUSE
FRB 20190102C	322.4157	-79.4757	0.2912	363.6	-106.1 ± 0.9	+26.6 ± 7.7	MUSE
FRB 20180924B ^a	326.1052	-40.9000	0.3212	362.2	+17.3 ± 0.8	+16.5 ± 5.0	2dF-AAOmega, MUSE
FRB 20211203C	204.5624	-31.3803	0.3439	635.0	+34.3 ± 1.2	-29.2 ± 9.1	MUSE
FRB 20200906A ^a	53.4962	-14.0832	0.3688	577.8	+75.4 ± 0.1	+30.3 ± 19.8	LRIS, DEIMOS, MUSE
FRB 20190611B	320.7456	-79.3976	0.3778	321.4	+17.0 ± 3.0	+29.0 ± 10.8	MUSE
FRB 20181112A	327.3485	-52.9709	0.4755	589.3	+10.5 ± 0.4	+16.2 ± 5.9	MUSE
FRB 20190711A	329.4192	-80.3580	0.5220	591.6	+4.0 ± 1.0	+19.4 ± 6.5	MUSE

^a part of the FLIMFLAM DR1 (Khrykin et al. 2024b; Huang et al. 2025)

^b DM measurements adopted from Bannister et al. (2019); Macquart et al. (2020); Heintz et al. (2020); Bhandari et al. (2020)

^c RM measurements adopted from Scott et al. (2025)

^d Milky Way RM contributions adopted from Hutschenreuter et al. (2022)

probe the properties of the magnetic field on different scales in the Universe (Akahori et al. 2016; Kovacs et al. 2024). For instance, observed FRB RMs can be used to constrain the magnetic field generated by the FRB progenitors (e.g., Piro & Gaensler 2018; Lyutikov 2022; Plavin et al. 2022; Anna-Thomas et al. 2023), refine Milky Way magnetic field constraints (Pandhi et al. 2025), or to shed light on the origin and strength of the magnetic field in the IGM, filaments and voids of the cosmic web (e.g., Hackstein et al. 2019; Padmanabhan & Loeb 2023; Mtchedlidze et al. 2024).

Of particular interest is to measure the strength of magnetic fields in galaxies, as these are interconnected with the processes of galaxy evolution and feedback (e.g. Bertone et al. 2006; Donert et al. 2009; Rodrigues et al. 2019). FRBs provide a promising new approach to investigate galactic magnetism, its amplification and evolution. For instance, Prochaska et al. (2019) discovered that the FRB 20181112A sightline passes through the halo of a foreground galaxy at $b_{\text{impact}} \simeq 29$ kpc. Through the analysis of the observed RM they reported an upper limit on the corresponding parallel component of the magnetic field in the galactic halo of $B_{\parallel} \leq 0.8 \mu\text{G}$ (assuming fiducial halo parameters). This estimate is at odds with previous high-redshift measurements that analysed the RM from a sample of Mg II absorbers at $\langle z \rangle = 1.3$ in quasar spectra, and found $B_{\parallel} \approx 10 \mu\text{G}$ in the CGM (Bernet et al. 2008). The small B_{\parallel} value found by Prochaska et al. (2019) can indicate a low-magnetized halo or a highly disordered magnetic field.

Recently, Mannings et al. (2023) analysed a sample of 9 FRBs and reported a positive correlation between DM and extragalactic RM_{e.g.} given by

$$\text{RM}_{\text{e.g.}} = \text{RM}_{\text{obs}} - \text{RM}_{\text{MW}}, \quad (1)$$

with RM_{obs} the observed RM and RM_{MW} an estimate for the Milky Way contribution. They concluded that majority of RM_{e.g.} thus must arise from the host galaxy. Sherman et al. (2023) expanded the sample to 25 FRBs and came to a similar conclusion,

emphasizing that the bulk of extragalactic RM_{e.g.} is coming from the ISM of the FRB hosts. However, these works assumed that only FRB progenitors and/or the ISM contribute to the observer RM_{obs}, ignoring any contribution from the halos of the FRB host galaxies. Moreover, they did not account for potential contribution to the observed RM_{obs} from intervening foreground halos. While searching for foreground halos requires extensive spectroscopic observations, ignoring this information can lead to erroneous conclusions (see Lee et al. 2023, for a similar discussion about DM_{FRB} in FRB 20190520B).

The goal of this work is to constrain and disentangle the magnetic fields in all galactic environments traversed by the FRB sightlines, including intervening foreground galactic halos. In order to do this, we build a large spectroscopic dataset of galactic halos in the foreground of well-localized FRBs, acquired by the FLIMFLAM collaboration (Lee et al. 2022; Simha et al. 2023; Khrykin et al. 2024b; Huang et al. 2025) and dedicated VLT/MUSE observations (PI: N. Tejos). We introduce a novel Bayesian Markov Chain Monte Carlo (MCMC) statistical framework, that takes into account both observational and modelling uncertainties, and recovers the magnetic field strength in various media along the FRB sightlines with high precision.

This paper is organized as follows. In Section 2, we outline the main properties of the FRB dataset analysed in this work. We discuss our model for the observed RM and each contributing component in Section 3. We summarize our Bayesian statistical model and present the results of the parameter inference in Section 4. We discuss our findings in Section 5 and conclude in Section 6. Throughout this work, we assume a flat Λ CDM cosmology with dimensionless Hubble constant $h = 0.673$, $\Omega_m = 0.315$, $\Omega_b = 0.046$, $\sigma_8 = 0.8$, and $n_s = 0.96$, consistent with the latest Planck results (Planck Collaboration et al. 2018).

2. Data Sample

In this work, we analyze a sample of 14 FRBs that were detected by the Commensal Real-time ASKAP Fast Transients (CRAFT;

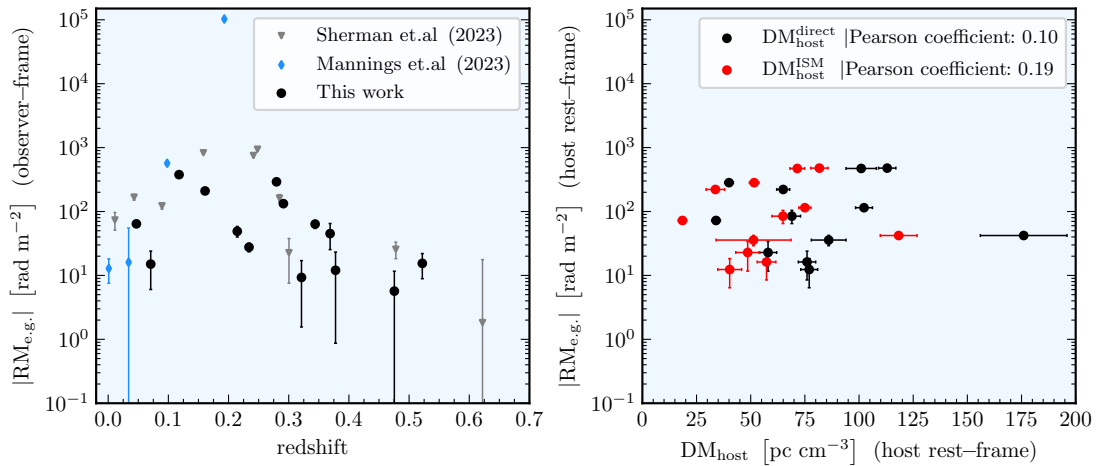


Fig. 1. (Left): The distribution of the absolute values of $RM_{e.g.}$ as a function of FRB redshift in observer frame. The black dots show the FRB sample analyzed in this work, whereas the gray triangles are the DSA-110 subsample taken from Sherman et al. (2023), and the blue diamonds illustrate the FRBs from Mannings et al. (2023) sample, which are not part of this work. (Right): The distribution of the $RM_{e.g.}$ values in the rest-frame of FRB hosts as a function of the corresponding $DM_{\text{host}}^{\text{direct}}$ and $DM_{\text{host}}^{\text{ISM}}$ values from Bernales-Cortes et al. (2025) (only for those, where corresponding MUSE data is available).

Macquart et al. 2010) survey conducted on the Australian Square Kilometre Array Pathfinder (ASKAP) radio telescope. The optical follow-up observations for host identification and redshift measurement were carried out in collaboration by the CRAFT and the Fast and Fortunate for FRB Follow-up¹ (F⁴) teams. We build the sample according to the following set of criteria: 1) the posterior probability of FRB-host association by the Probabilistic Association of Transients to their Hosts (PATH; Aggarwal et al. 2021) algorithm must be $P(O|x) \geq 0.95$; 2) the FRB must have a publicly available RM measurement; and 3) a given FRB field must have available spectroscopic observations of foreground galaxies. We summarize the main properties of the FRBs in the sample in Table 1 noting that the RM_{obs} values adopted here are all taken from Scott et al. (2025).

The left-hand panel of Figure 1 shows the estimated extragalactic $RM_{e.g.}$, using eq. (1) and an estimate for RM_{MW} (see Table 1), in our sample as a function of the FRB redshift. Meanwhile, the right-hand panel illustrates the distribution of $RM_{e.g.}$ as a function of the estimated dispersion measure $DM_{\text{host}}^{\text{direct}}$ associated with the host galaxies (halo+ISM/FRB progenitor) of the FRBs in the sample. We also show $DM_{\text{host}}^{\text{ISM}}$ estimates separately by the red markers. The values are adopted from the analysis of $H\alpha$ flux and halo masses in the FRB hosts by Bernales-Cortes et al. (2025). We run a Pearson correlation test between the $RM_{e.g.}$ and $DM_{\text{host}}^{\text{direct}}$ and between $RM_{e.g.}$ and $DM_{\text{host}}^{\text{ISM}}$ values and find no significant correlation in either case with $r_{\text{pearson}} = 0.10$ ($r_{\text{pearson}} = 0.19$).

We require foreground spectroscopic information in each FRB field in order to identify and characterize galaxies that are intersected by the FRB sightlines in our sample, and that might contribute to the observed RM_{obs} . Recently, the FLIMFLAM survey (Khrykin et al. 2024b; Huang et al. 2025) has acquired large spectroscopic samples of galaxies in the foreground of 8 localized FRBs utilized in the FRB foreground mapping approach (Lee et al. 2022) to infer the distribution of cosmic baryons. For 7 of the 14 FRBs in our sample, which are also part of FLIMFLAM DR1 (Khrykin et al. 2024b), we adopt their narrow-field spectroscopic data (within $10''$ of the FRB sightlines; see

Huang et al. 2025). These observations were performed with the AAOmega spectrograph on the Anglo-Australian Telescope (Smith et al. 2004), the Low-Resolution Imaging Spectrograph (LRIS; Rockosi et al. 2010), the DEep Imaging Multi-Object Spectrograph (DEIMOS; Faber et al. 2003), and the integral field unit (IFU) Keck Cosmic Web Imager (KCWI; Morrissey et al. 2018) on the Keck Telescopes at the W. M. Keck Observatory, and the IFU Multi-Unit Spectroscopic Explorer (MUSE; Bacon et al. 2010) on the Very Large Telescope (VLT). We refer the interested reader to Huang et al. (2025) for more detailed descriptions of these observations. For the remaining 7 FRB fields in our sample lacking FLIMFLAM observations, we used MUSE to obtain the spectra of galaxies within the $1 \times 1 \text{ arcmin}^2$ field of the respective FRB positions. Each FRB field has been observed for $4 - 8 \times 800 \text{ s}$ with MUSE to reach $r \lesssim 25$ sources (Bernales-Cortes et al. 2025).

Furthermore, we obtain photometric information on identified foreground galaxies by querying publicly available imaging surveys including the Dark Energy Survey (DES; Abbott et al. 2021), the DECam Local Volume Exploration survey (DELVE; Drlica-Wagner et al. 2022), and the the Panoramic Survey Telescope and Rapid Response System (Pan-STARRS; Chambers et al. 2016). For MUSE sources without data in existing public imaging surveys, we construct synthetic photometry adopting SDSS g , r , and i filters, but manually setting the transmission to zero beyond the MUSE wavelength range of $4800 - 9300 \text{ \AA}$. Additionally, we set the transmission to zero in the $5800 - 5960 \text{ \AA}$ wavelength window in order to account for the blocking filter used to avoid the light from the laser guide stars. This photometric information is then used to estimate the corresponding stellar masses of identified galaxies via spectral energy distribution (SED) fitting. For this purpose, we adopt the publicly available SED fitting algorithm CIGALE (Boquien et al. 2019) with the initialization parameters previously used by Simha et al. (2023) and Khrykin et al. (2024b). In what follows, we adopt the mean stellar masses of foreground galaxies estimated by CIGALE, and use the average stellar-to-halo mass relation of Moster et al. (2013) to convert to the corresponding halo masses, M_{halo} , at a given redshift.

¹ <https://sites.google.com/ucolick.org/f-4>

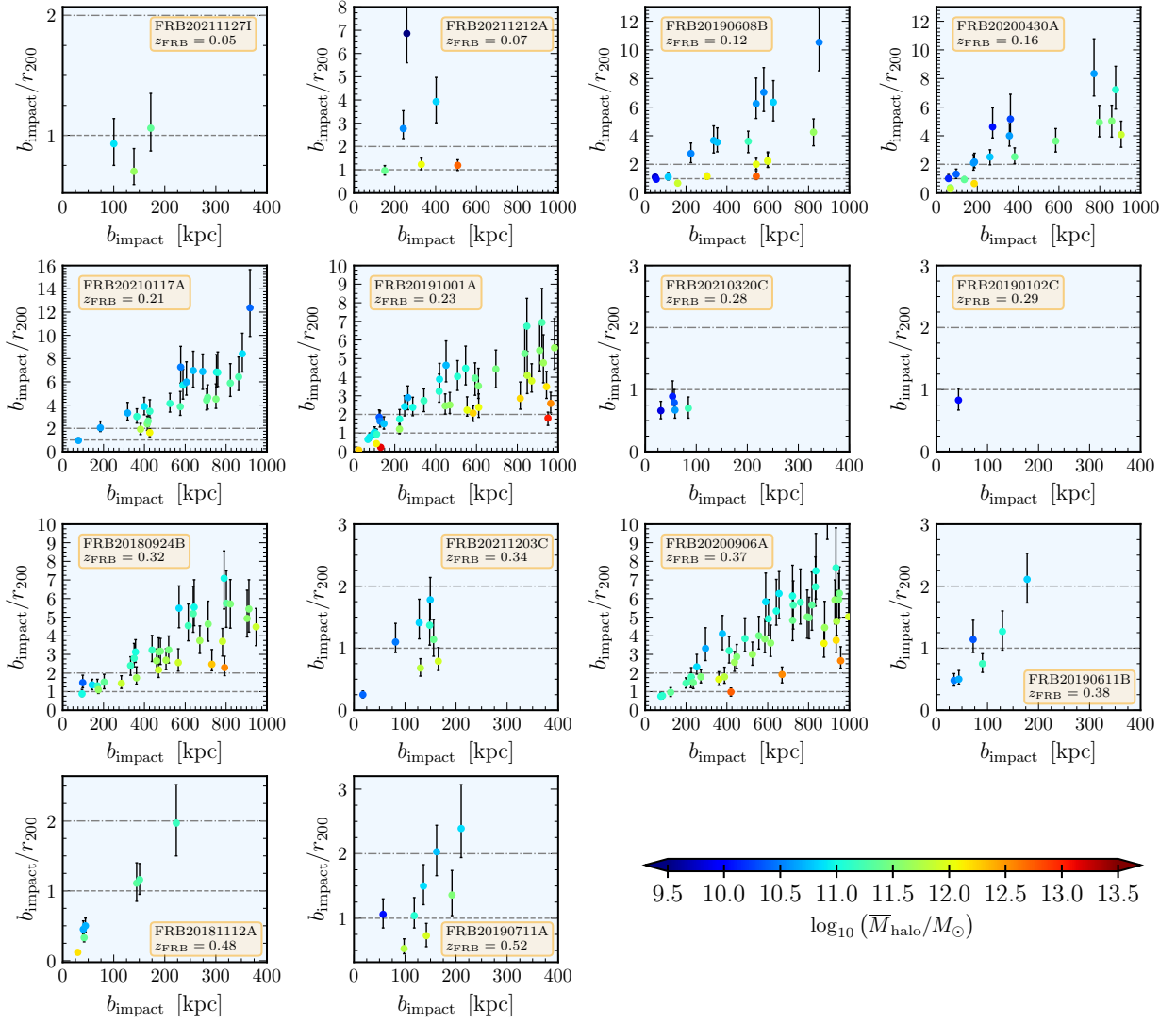


Fig. 2. The impact parameter b_{impact} of identified foreground halos with respect to their virial radius r_{200} along each FRB sightline, plotted as a function of the impact parameter. The colormap illustrates the mean mass of the halos, whereas the associated uncertainty is propagated into the errorbars on their corresponding r_{200} . The dashed line illustrates the maximum distance $b_{\text{impact}} = r_{200}$, at which a foreground halo can be intersected by the FRB sightline and potentially contribute to RM_{obs} if halo extends to 1 virial radii, r_{200} . In addition, we also show the case when the halos extend to two virial radii $2 \times r_{200}$ with the dash-dotted lines.

Figure 2 illustrates all halos of galaxies and groups that were observed in the foreground of each FRB in our sample. Those halos that are located at impact parameters b_{impact} less of equal to their respective virial radii r_{200} can contribute to the observed RM_{obs} .

3. Rotation Measure Model

Rotation measure is one of the key observables of the FRB signal. It represents the change in the polarization angle of the Faraday rotated polarized emission propagated through the intervening ionized and magnetized gas. While DM quantifies the integrated number density of free electrons along the propagation path of a signal, RM describes the same integral but weighted by the line-of-sight (parallel) component of the magnetic field, B_{\parallel} :

$$\text{RM}_{\text{obs}} = \int \frac{B_{\parallel} n_e}{(1+z)^2} dz. \quad (2)$$

As an integral quantity, RM_{obs} can be described as a sum of contributions from several components along the FRB line-of-sight. Thus, for each i th FRB in our sample we consider the following model for RM_{obs} in the observer frame:

$$\text{RM}_{\text{model},i} = \text{RM}_{\text{MW},i} + \text{RM}_{\text{IGM},i} + \sum_j^{N_{\text{f/g}}} \text{RM}_{\text{f/g},ij}^{\text{halo}} + \text{RM}_{\text{host},i}, \quad (3)$$

where $\text{RM}_{\text{MW},i}$ corresponds to the contribution from the halo and ISM of the Milky Way (see Table 1), $\text{RM}_{\text{IGM},i}$ arises from the diffuse gas in the IGM, $\text{RM}_{\text{f/g},ij}^{\text{halo}}$ is the contribution from the individual intervening foreground galactic halos, $N_{\text{f/g}}$ is the number of intersected foreground halos, and $\text{RM}_{\text{host},i}$ comes from the FRB host galaxies. In what follows, we discuss each of these components in detail.

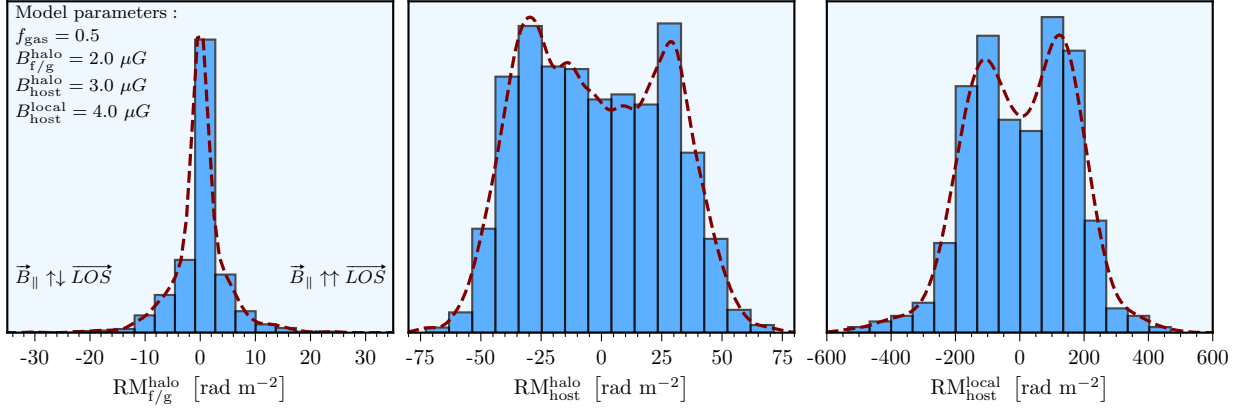


Fig. 3. Example of the typical distributions of RM values for FRB 20111212A: (*left*) from the mNFW model of a single foreground galactic halo (see Section 3.3); (*middle*) from the mNFW model of the corresponding host galaxy halo (see Section 3.4.1); (*right*) from the local environment in the ISM of the host galaxy and/or FRB progenitor (see Section 3.4.2). The positive values of the histograms, correspond to the RM values for the case when the line of sight component of the magnetic field is aligned with the direction of the FRB sightline (parallel), whereas the negative parts of the histograms, illustrate the case when the line of sight component of the magnetic field is directed away from the observer (antiparallel). The dashed maroon lines show the KDE fit to the resulting RM distributions (see Section 4). Note the different range of RM values in the panels.

3.1. The Milky Way

The contribution from the Milky Way, RM_{MW} , arises both from the magnetized and ionized gas in the Galactic halo and from the ISM within the disk. In this work, we adopt the all-sky Faraday rotation map model from Hutschenreuter et al. (2022), based on $\sim 55\,000$ Faraday rotation sources compiled from multiple radio surveys (e.g. LOFAR Two-meter Sky Survey and NRAO VLA Sky Survey RM catalogue). The map provides a RM_{MW} measurement with associated uncertainty for a given position on the sky. We list the resulting RM_{MW} values for each FRB field in Table 1 (see also Pandhi et al. 2025).

3.2. The Intergalactic Medium

Due to expected multiple reversals of the intergalactic magnetic field, the RM_{IGM} , arising from the low-density IGM gas tracing the large-scale structure (LSS) of the Universe, is expected to be small relative to other contributing environments (see Eq. 3). Recent LOFAR measurement of $\langle RM \rangle \approx 0.71 \pm 0.07 \text{ rad m}^{-2}$ in LSS filaments is consistent with magnetic field of $\approx 32 \text{ nG}$ (e.g., Amaral et al. 2021; Pomakov et al. 2022; Carretti et al. 2022, 2023, and the references within). Given that this RM_{IGM} value is at least 1 – 2 orders of magnitude smaller, than the RM_{obs} and RM_{MW} (see Table 1), for the remainder of the paper we assume that the IGM contribution is negligible, i.e. our model adopts

$$RM_{IGM} = 0 \text{ rad m}^{-2} \quad (4)$$

3.3. The Foreground Halos

In order to estimate the electron density and RM contribution of a given foreground halo intersected by the FRB sightline, we utilize the modified Navarro-Frank-White model (mNFW; Prochaska & Zheng 2019). This model yields a radial density profile $\rho_b(r)$ of the gas in individual halos given by

$$\rho_b(r) = f_{\text{gas}} \frac{\Omega_b}{\Omega_m} \frac{\rho_0(M_{\text{halo}})}{y^{1-\alpha} (y_0 + y)^{2+\alpha}}, \quad (5)$$

where f_{gas} is the fraction of cosmic baryons located in the ionized CGM relative to the total amount of baryons within individual galactic halos; ρ_0 is the central density of the halo as a function of halo mass, M_{halo} ; $y \equiv c(r/r_{200})$, where c is the concentration parameter, while y_0 and α are mNFW model parameters. Here we adopt the fiducial values $y_0 = \alpha = 2$ from Prochaska & Zheng (2019), while considering f_{gas} as a free parameter. All identified foreground galaxies and groups are illustrated in Figure 2, where we plot the ratio of the halo impact parameter to the corresponding virial radius r_{200} as a function of the impact parameter.

The $RM_{f/g}^{\text{halo}}$ contribution of an individual halo in units of rad m^{-2} is obtained by integrating the density profile $\rho_b(r)$ given by eq. (5) as

$$RM_{f/g}^{\text{halo}} = \frac{B_{f/g}^{\text{halo}} \cos \alpha_{f/g} e^3 \mu_e}{2\pi m_e^2 c^4 m_p \mu_H} 2 \int_0^{\sqrt{r_{\text{max}}^2 - r_{\perp}^2}} \rho_b(s) ds, \quad (6)$$

(e.g., Akahori & Ryu 2011), where e and m_e are the electric charge and mass of the electron, c is the speed of light, m_p is the mass of the proton, $\mu_H = 1.3$ and $\mu_e = 1.167$ take into account both hydrogen and helium atoms; r_{\perp} is the impact parameter of the FRB sightline with respect to the centre of the halo, and r_{max} is the maximum extent of the halo in units of r_{200} , and s is the path that FRB follows inside a given halo. In what follows, we adopt a fixed $r_{\text{max}} \equiv r_{200}$ value, similar to the approach in Khrykin et al. (2024b)². The term $B_{f/g}^{\text{halo}}$ describes the average strength of the total magnetic field in the foreground galactic halos in units of μG , and it is one of the free parameters we consider in this work. In what follows, we assume $B_{f/g}^{\text{halo}}$ is constant with respect to r . Furthermore, $B_{f/g}^{\text{halo}}$ is multiplied by the cosine of the angle $\alpha_{f/g}$ between the direction of the magnetic field vector and line-of-sight in order to obtain the required parallel component

² In principle, r_{max} should also be included as another free parameter (see Prochaska & Zheng 2019; Simha et al. 2020; Lee et al. 2023). However, we tested the model using $r_{\text{max}} = 2 \times r_{200}$ and did not find significant differences in the results. Therefore, in this work, we adopt a fixed truncation radius and will explore a more sophisticated parametrization in the future.

(see eq. 3). We note that $\text{RM}_{\text{f/g}}^{\text{halo}}$ in eq. (6) is defined in the rest-frame of each foreground halo. We, therefore, additionally multiply eq. (6) by a $(1 + z_{\text{halo}})^{-2}$ to account for the redshift dilation and convert the result to the observer frame.

In addition, both the stellar mass estimate and the stellar-to-halo mass relation, are subjects of considerable uncertainties. Similar to Khrykin et al. (2024b), we take these uncertainties into account by introducing a random scatter of 0.3 dex to the inferred mass of each halo (see Simha et al. 2021 for more details). For each foreground halo, we construct a log-normal distribution of its halo mass adopting the corresponding mean and standard deviation values. We then randomly draw $N = 1000$ realizations of the halo mass from this distribution. Additionally, in order to account for the orientation of the magnetic field, for each draw we randomly choose an angle $\alpha_{\text{f/g}}$ from the uniform distribution $\mathcal{U}[0, \pi]$, and calculate the corresponding $\text{RM}_{\text{f/g}}^{\text{halo}}$ value given by eq. (6).

An example of the model distribution of $\text{RM}_{\text{f/g}}^{\text{halo}}$ values for a single foreground halo located at $b_{\text{impact}} = 150$ kpc away from the FRB 20211212A sightline is illustrated by the histogram in the left panel of Figure 3. It is apparent, that the $\text{RM}_{\text{f/g}}^{\text{halo}}$ histogram is centered around the $\text{RM} \approx 0$ rad m⁻². In the particular case of this foreground halo, for the majority of the halo mass realizations, the extent of the halo, r_{200} , is smaller than the corresponding impact parameter of the halo ($b_{\text{impact}} = 150$ kpc, see Figure 2). Therefore, in those realizations where the sightline does not actually intersect the foreground halo the resulting $\text{RM}_{\text{f/g}}^{\text{halo}}$ is effectively zero.

3.4. The FRB Host Galaxy

The contribution from the FRB host galaxies to the observed RM_{obs} remains highly uncertain. Previous studies analyzing the FRB RMs did not have information about the foreground large scale structures (LSS) and galactic halos, attributing all the extragalactic RM (after subtracting the contribution from the Milky Way) to the FRB hosts. Moreover, some previous works assumed that all of the host contribution arises only from the ISM or local FRB environment, ignoring potential contributions from the extended halo of the host galaxy (e.g., Mannings et al. 2023). In this work, we attempt to explicitly model both the halo and local contributions from the FRB hosts, employing the following model:

$$\text{RM}_{\text{host}} = \frac{\text{RM}_{\text{host}}^{\text{halo}} + \text{RM}_{\text{host}}^{\text{local}}}{(1 + z_{\text{host}})^2}, \quad (7)$$

where $\text{RM}_{\text{host}}^{\text{halo}}$ describes the contribution from the halo of the FRB host galaxy, and $\text{RM}_{\text{host}}^{\text{local}}$ denotes the contribution from the FRB progenitor itself and/or the ISM environment of the host galaxy, in which the progenitor resides. Here, similar to the foreground galaxies, we rescale RM_{host} to the observer frame by a factor $(1 + z_{\text{host}})^{-2}$. In what follows, we describe the calculation of each of these terms separately.

3.4.1. The Host Halo

In order to estimate the $\text{RM}_{\text{host}}^{\text{halo}}$ for a given FRB in our sample, we follow the discussion in Section 3.3 and similarly adopt the mNFW model. We utilize publicly available estimates of the host stellar masses from Gordon et al. (2023) to describe their halo radial density profiles $\rho_b(r)$. We then obtain the value of

the $\text{RM}_{\text{host}}^{\text{halo}}$ by integrating $\rho_b(r)$ using eq. 6. However, contrary to the $\text{RM}_{\text{f/g}}^{\text{halo}}$ case, we integrate only over the half of the host halo as

$$\text{RM}_{\text{host}}^{\text{halo}} = \frac{B_{\text{host}}^{\text{halo}} \cos \alpha_{\text{hh}} e^3 \mu_e}{2\pi m_e^2 c^4 m_p \mu_H} \int_0^{\sqrt{r_{\text{max}}^2 - r_1^2}} \rho_b(s) ds, \quad (8)$$

where $B_{\text{host}}^{\text{halo}}$ is the the average strength of the total magnetic field in the halos of the FRB hosts in units of μG , and it is another free parameter considered in this work. Similar to discussion in Section 3.3, we assume $B_{\text{host}}^{\text{halo}}$ is constant with respect to location r in the halo. α_{hh} is the angle between the direction of the $B_{\text{host}}^{\text{halo}}$ vector and the line-of-sight.

We take into account the uncertainty in the halo masses by introducing a random 0.3 dex scatter and perform a Monte Carlo sampling ($N = 1000$ draws) of the corresponding log-normal distribution of the FRB hosts halo masses. Similar to the $\text{RM}_{\text{f/g}}^{\text{halo}}$ calculations in Section 3.3, for each halo mass realization we draw a value of α_{hh} from the corresponding uniform distribution $\alpha_{\text{hh}} \in \mathcal{U}[0, \pi]$ to take into account the orientation of the magnetic field relative to the line-of-sight. This procedure results in a distribution of $\text{RM}_{\text{host}}^{\text{halo}}$ values for each host in the sample. An example of such a distribution for the halo of the FRB 20211212A host galaxy is illustrated in the middle panel of Figure 3.

3.4.2. The Host ISM/FRB Progenitor

To describe the RM associated either with the FRB source itself or with the host galaxy ISM (or both), which we term $\text{RM}_{\text{host}}^{\text{local}}$, we utilize the RM-DM relation (Akahori et al. 2016; Pandhi et al. 2022), which after accounting for all the constants is given by (in host rest-frame)

$$\text{RM}_{\text{host}}^{\text{local}} = \frac{B_{\text{host}}^{\text{local}} \cos \alpha_{\text{hl}} \text{DM}_{\text{host}}^{\text{local}}}{1.22}, \quad (9)$$

where $\text{DM}_{\text{host}}^{\text{local}}$ is the rest-frame dispersion measure in the local FRB environment in units of pc cm⁻³, the $B_{\text{host}}^{\text{local}}$ is the average strength of the total magnetic field associated with ISM/progenitor in units of μG , and α_{hl} is the angle between the direction of the $B_{\text{host}}^{\text{local}}$ vector and the line-of-sight. In what follows, we consider $B_{\text{host}}^{\text{local}}$ as another free parameter in our model.

Recently, the analysis of the FLIMFLAM DR1 (Khrykin et al. 2024b; Huang et al. 2025) yielded the first ever published direct estimate of $\text{DM}_{\text{host}}^{\text{local}}$ (DM contribution from the FRB progenitor and/or host ISM), inferring an average contribution of $\text{DM}_{\text{host}}^{\text{local}} = 69_{-19}^{+28}$ pc cm⁻³. We adopt these findings and draw $N = 1000$ realizations of $\text{DM}_{\text{host}}^{\text{local}}$ from the corresponding 1D posterior PDF from Khrykin et al. (2024b). Similar to the discussion in Sections 3.3 and 3.4.1, we sample the uniform distribution $\alpha_{\text{hl}} \in \mathcal{U}[0, \pi]$ in order to take into account the orientation of the $B_{\text{host}}^{\text{local}}$ vector relative to the FRB sightline. The resulting $\text{RM}_{\text{host}}^{\text{local}}$ distribution for FRB 20211212A, calculated using eq. (9), is illustrated by the histogram in the right-hand panel of Figure 3.

4. Statistical Inference

In order to estimate the set of model parameters $\Theta = \{f_{\text{gas}}, B_{\text{f/g}}^{\text{halo}}, B_{\text{host}}^{\text{halo}}, B_{\text{host}}^{\text{local}}\}$ and associated uncertainties, we adopt a

Bayesian inference formalism. Therefore, first, we need to define the Bayesian likelihood function $\mathcal{L}_{\text{FRB}}(\text{RM}_{\text{obs},i}|\Theta)$ for the observed $\text{RM}_{\text{obs},i}$ given Θ for each i th FRB in the sample.

4.1. The Likelihood Function

We begin by constructing a grid of parameter values on which the likelihood will be estimated. For f_{gas} we adopt a range $f_{\text{gas}} = [0.01, 1.0]$ with step $\Delta = 0.1$. Further, we assume the same range for the strength of the magnetic field in three environments $B \equiv B_{\text{f/g}}^{\text{halo}} \equiv B_{\text{host}}^{\text{halo}} \equiv B_{\text{host}}^{\text{local}} = [0, 20] \mu\text{G}$ with step $\Delta = 0.5 \mu\text{G}$.

Having defined the parameter grid, we obtain the values of the likelihood function $\mathcal{L}_{\text{FRB}}(\text{RM}_{\text{obs},i}|\Theta)$ for a single i th FRB at each point of the parameter grid following the algorithm from Khrykin et al. (2021) as follows:

1. Given the $B_{\text{f/g}}^{\text{halo}}$ and $B_{\text{host}}^{\text{halo}}$ values in Θ we calculate the corresponding distributions of $\text{RM}_{\text{f/g},i}^{\text{halo}}$ and $\text{RM}_{\text{host},i}^{\text{halo}}$, respectively (see Section 3.3 and 3.4.1). Note that for each foreground or FRB host halo we perform a new random draw from the corresponding uniform distribution describing the orientation angles of a given magnetic field vector. We fit each of these distributions with a Kernel Density Estimator (KDE; maroon dashed lines in the left-hand and middle panels of Figure 3), and then resample them by randomly drawing $N = 2000$ realizations of $\text{RM}_{\text{f/g}}^{\text{halo}}$ and $\text{RM}_{\text{host}}^{\text{halo}}$ values.
2. Given the value of $B_{\text{host}}^{\text{local}}$ and assuming the FLIMFLAM estimates of $\text{DM}_{\text{host}}^{\text{local}}$ we calculate a distribution of $\text{RM}_{\text{host},i}^{\text{local}}$ values following eq. (9). Similarly, to the previous step (1), we fit the resulting distribution with the KDE (maroon dashed line in the right-hand panel of Figure 3) and randomly draw $N = 2000$ values of $\text{RM}_{\text{host}}^{\text{local}}$.
3. Given the value of $\text{RM}_{\text{MW},i}$ and the associated 1σ uncertainty (see Table 1), we construct a corresponding Gaussian distribution from which we randomly draw $N = 2000$ realizations of RM_{MW} .
4. We calculate the joint distribution of $\text{RM}_{\text{model},i}$ values given by eq. (3) by adding together $N = 2000$ RM samples obtained through steps (1)-(3). An example of such joint $\text{RM}_{\text{model},i}$ distribution for a single realization of Θ for FRB 20211212A is shown by the histogram in Figure 4.
5. We apply the KDE to the resulting joint $\text{RM}_{\text{model},i}$ distribution to find its continuous probability density function (PDF; see maroon dashed line in Figure 4). Finally, we estimate the value of the likelihood function by evaluating the resulting total KDE PDF at the observed value of the $\text{RM}_{\text{obs},i}$ for a given FRB (see Table 1 and vertical magenta line in Figure 4).
6. We repeat steps (1)-(5) for each combination of model parameters, Θ .

This procedure results in $N = N_{f_{\text{gas}}} N_B^3 = 758131$ determinations of the likelihood function $\mathcal{L}_{\text{FRB}}(\text{RM}_{\text{obs},i}|\Theta)$ evaluated on $\Theta \equiv \{f_{\text{gas}}, B_{\text{f/g}}^{\text{halo}}, B_{\text{host}}^{\text{halo}}, B_{\text{host}}^{\text{local}}\}$ parameter grid for each FRB in the sample. Next, we obtain a joint likelihood function for the entire sample by taking the product of the individual (independent) likelihood functions

$$\mathcal{L}_{\text{joint}} = \prod_i^{N_{\text{FRB}}} \mathcal{L}_{\text{FRB}}(\text{RM}_{\text{obs},i}|\Theta), \quad (10)$$

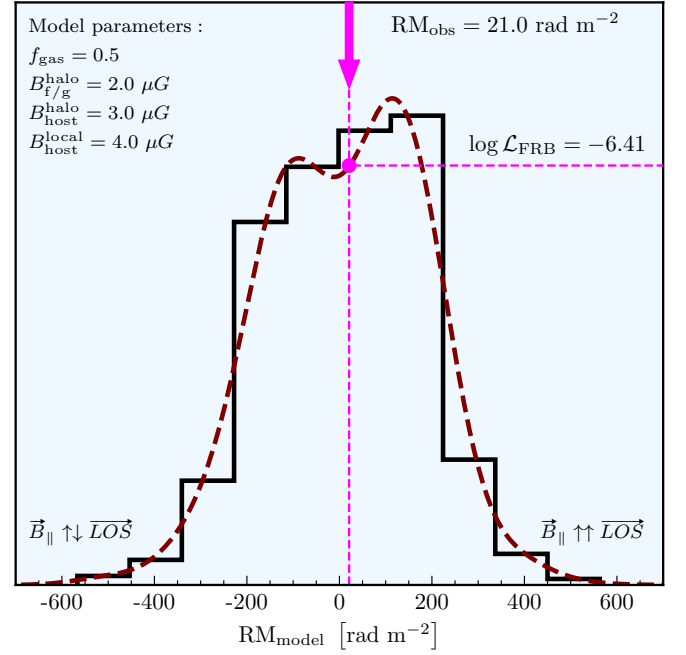


Fig. 4. Resulting distribution of the RM_{model} values given by eq. (3), estimated by combining contributions from each environment along the FRB sightline (see Section 3 and Figure 3 for details). The vertical magenta dashed line illustrates the value of the RM_{obs} for FRB 20211212A, while the horizontal magenta dotted line shows the value of the corresponding log-likelihood value ($\log \mathcal{L}_{\text{FRB}} = -6.41$) evaluated from the KDE fit to the RM_{model} distribution at the value of RM_{obs} , given the combination of model parameters Θ (see discussion in Section 4 for more details).

where $N_{\text{FRB}} = 14$ is the number of FRBs in our sample (see Table 1).

Finally, we interpolate $\mathcal{L}_{\text{joint}}$ given by eq. (10) for any arbitrary combination of parameter values that lie between the grid points of the parameter space.

4.2. The Priors

As in any Bayesian inference, it is important to be explicit about the adopted priors π on our model parameters, which we define in what follows. First, giving the lack of observational information, we adopt a flat uniform non-informative prior on the fraction of cosmic baryons in the galactic halos, f_{gas} , i.e., $\pi(f_{\text{gas}}) = (0, 1]$. Similarly, we use a flat uniform prior for each of the magnetic fields, $\pi(B_{\text{f/g}}^{\text{halo}}) = \pi(B_{\text{host}}^{\text{halo}}) = \pi(B_{\text{host}}^{\text{local}}) = [0, 20] \mu\text{G}$ (e.g. Beck & Wielebinski 2013). Moreover, given the difference in the densities in the halos and ISM environment of the galaxies, we set the following extra condition $B_{\text{f/g}}^{\text{halo}} < B_{\text{host}}^{\text{local}}$ and, analogously, $B_{\text{host}}^{\text{halo}} < B_{\text{host}}^{\text{local}}$. This is consistent with the expectations from magneto-hydrodynamic simulations (e.g. Ramesh et al. 2023).

In addition, following Khrykin et al. (2024b) we adopt a prior on the total budget of cosmic baryons in the diffuse states outside of the individual galaxies, f_d , as

$$f_d(z) \equiv f_{\text{igm}} + f_{\text{cgm}} + f_{\text{icm}} = 1 - f_{\text{stars}} - f_{\text{bh}} - f_{\text{ism}}, \quad (11)$$

where f_{igm} is the fraction of cosmic baryons residing in the diffuse IGM gas, f_{icm} is the fraction of cosmic baryons inside the intracluster media (ICM) of galaxy clusters with $M_{\text{halo}} \geq 10^{14} M_{\odot}$,

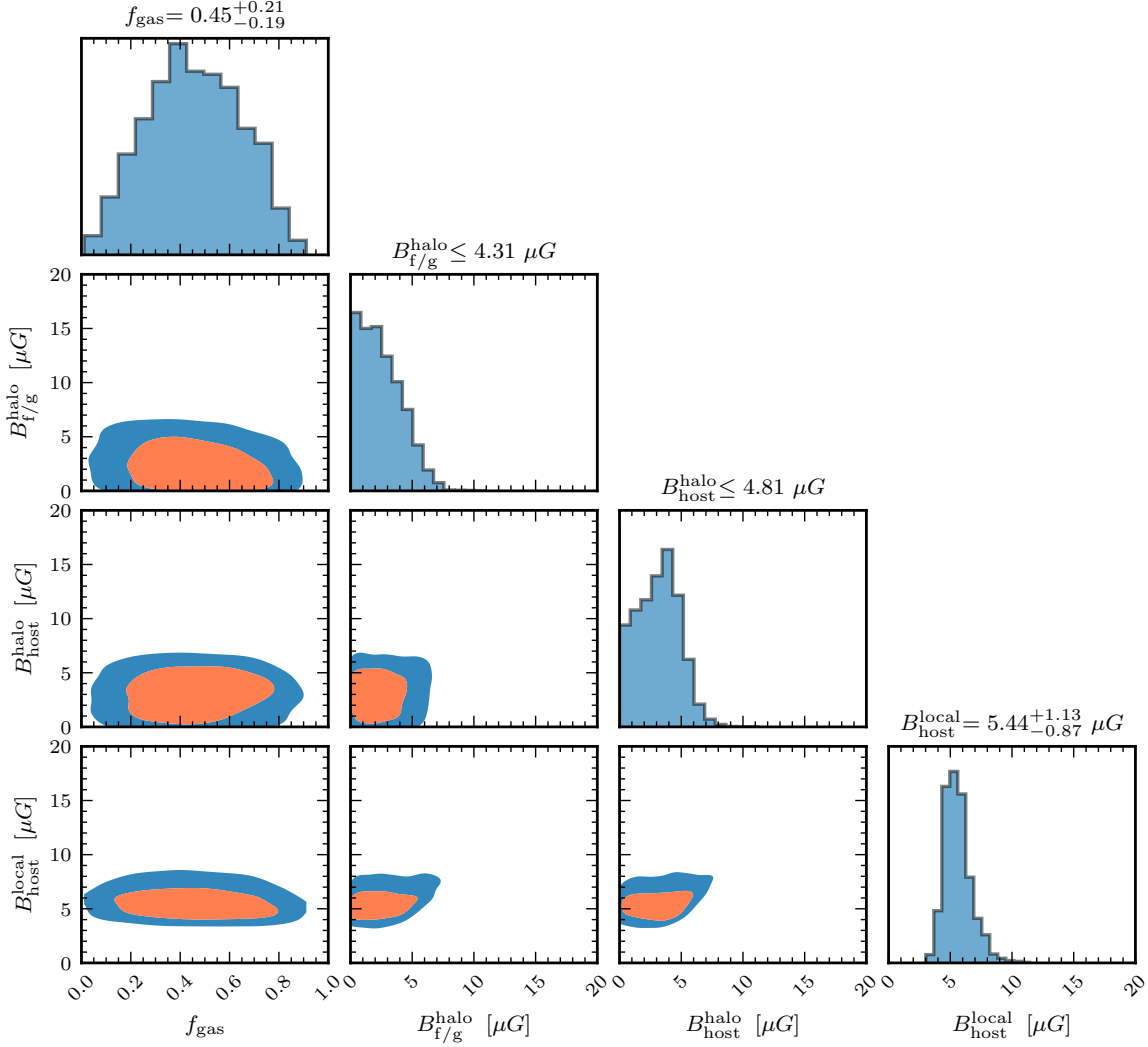


Fig. 5. MCMC inference result for the sample of 14 FRBs in our dataset (see Table 1). The orange (blue) contours correspond to the inferred 68% (95%) confidence intervals. The diagonal panels show the corresponding marginalized 1D posterior probabilities of the model parameters.

while f_{cgm} is the cosmic baryon fraction in all the halos at $M_{\text{halo}} < 10^{14} M_{\odot}$; in contrast to f_{gas} , which represents the average fraction of the ionized CGM baryons in the individual halos, f_{cgm} represents the fraction of baryons integrated over all CGM in the Universe. We follow the discussion in Macquart et al. (2020) to estimate the $f_d(z)$, and refer the interested reader to the full description provided in Khrykin et al. (2024b). Given the uncertainties in the stellar IMF, evaluating $f_d(z)$ at the mean redshift of our FRB sample $\langle z_{\text{sample}} \rangle \simeq 0.27$, yields $f_d(z = 0.27) \simeq 0.86 \pm 0.02$.

In what follows, we assume $f_{\text{igm}} = 0.59 \pm 0.10$, which is the value found in the FLIMFLAM DR1 analysis by Khrykin et al. (2024b). Following the approach in that work, we calculate the look-up conversion table between f_{gas} and f_{cgm} by integrating the Aemulus halo mass function (McClintock et al. 2019) over the mass range of the halos in our sample, $10 \lesssim \log_{10}(M_{\text{halo}}/M_{\odot}) \lesssim 13.1$ (this includes both foreground and FRB host halos). A similar conversion is adopted between $f_{\text{gas}}^{\text{icm}}$ and f_{icm} assuming $M_{\text{halo}} \geq 10^{14} M_{\odot}$ and $f_{\text{gas}}^{\text{icm}} = 0.8 \pm 0.1$, consistent with measurements of gas in galaxy clusters (Gonzalez et al. 2013; Chiu et al. 2018).

Additionally, we note that our sample of foreground (see Figure 2) and FRB hosts halos does not cover the full range of halo masses below the cluster mass limit of $M_{\text{halo}} \simeq 10^{14} M_{\odot}$. Therefore, we split f_{cgm} into $f_{\text{cgm}}^{\text{sample}}$ representing the halo mass range of our sample, and $f_{\text{cgm}}^{\text{other}}$ corresponding to the halo mass range of $13.1 \leq \log_{10}(M_{\text{halo}}/M_{\odot}) < 14.0$ not covered by our data. Consequently, at each step of the MCMC inference, the proposed value of f_{gas} is converted to $f_{\text{cgm}}^{\text{sample}}$ using the precomputed lookup table. For the non-cluster halo mass range not covered by our data, we randomly pick a value of f_{gas} for these halos from the uniform distribution $\mathcal{U}(0, 1]$ and convert into the corresponding $f_{\text{cgm}}^{\text{other}}$ fraction also adopting the Aemulus halo mass function. These terms, together with mean value of f_{icm} , are then compared to the range of the $f_d(z)$ in eq. (11), yielding the following prior:

$$\langle f_d \rangle - \sigma_{\text{tot}} \leq \langle f_{\text{igm}} \rangle + f_{\text{cgm}}^{\text{sample}} + f_{\text{cgm}}^{\text{other}} + \langle f_{\text{icm}} \rangle \leq \langle f_d \rangle + \sigma_{\text{tot}}, \quad (12)$$

where σ_{tot} takes into account the corresponding uncertainties in f_d , f_{igm} , and f_{icm} , and is given by

$$\sigma_{\text{tot}} = \sqrt{\sigma_{f_d}^2 + \sigma_{f_{\text{igm}}}^2 + \sigma_{f_{\text{icm}}}^2} \approx 0.14 \quad (13)$$

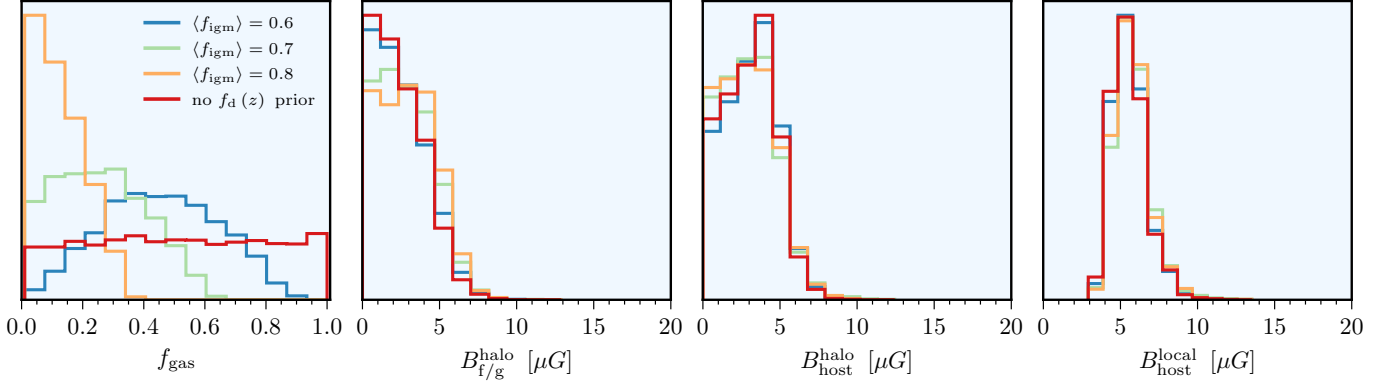


Fig. 6. 1D marginalized posterior probability distributions of model parameters considered in this work, estimated with different value of $\langle f_{\text{igm}} \rangle$ adopted for the $f_d(z)$ prior (see Section 4.2). The fiducial model with $\langle f_{\text{igm}} \rangle = 0.60$ is shown by the blue curves.

4.3. Inference results

Given the expression for the joint likelihood function described in Section 4.1 and the choice of priors in Section 4.2, we now proceed to sample this $\mathcal{L}_{\text{joint}}$. In what follows, we adopt the publicly available affine-invariant MCMC sampling algorithm EMCEE by Foreman-Mackey et al. (2013) to obtain the posterior probability distributions for our model parameters.

The resulting posterior PDFs of the four model parameters $\Theta \equiv \{f_{\text{gas}}, B_{\text{f/g}}^{\text{halo}}, B_{\text{host}}^{\text{halo}}, B_{\text{host}}^{\text{local}}\}$ are illustrated in Figure 5, where the red (blue) contours correspond to the 68% (95%) confidence intervals (CI), whereas the marginalized 1D posterior PDFs for each of the model parameters are shown in the diagonal top panels. It is apparent upon inspection of the marginalized posterior PDFs, that for some of the considered model parameters we can only place upper limits, whereas for the others we are able to make a measurement. In order to distinguish between these two cases we adopt the following criterion. If the peak of the posterior PDF is at least four times larger than the larger of the two posterior PDF values at the edges of the corresponding parameter range, then we classify it as a measurement. We then quote the median 50th percentile of the marginalized posterior distributions as the measured values, while the corresponding uncertainties are estimated from the 16th and 84th percentiles, respectively. On the other hand, if the above criterion is not met, we report an upper limit by quoting the 84th percentile (effectively, 1σ) of the posterior PDF for a given parameter.

Given our choice of priors in Section 4.2, we estimate the average strength of the magnetic field inside the ISM and/or FRB progenitor to be $B_{\text{host}}^{\text{local}} = 5.44^{+1.13}_{-0.87} \mu\text{G}$. On the other hand, we are able to only place the upper limit on the average strength of the magnetic field in the FRB host halos because the $B_{\text{host}}^{\text{halo}} \simeq 0.0 \mu\text{G}$ has a significant posterior probability. Our inference yields $B_{\text{host}}^{\text{halo}} \lesssim 4.81 \mu\text{G}$. Similarly, we place an upper limit on the average strength of the magnetic field in foreground halos, $B_{\text{f/g}}^{\text{halo}} \lesssim 4.31 \mu\text{G}$. Finally, we infer the fraction of cosmic baryons inside individual galactic halos to be $f_{\text{gas}} = 0.45^{+0.21}_{-0.19}$. Following the discussion in Section 4.2 (see Khrykin et al. 2024a, for more details), this implies that a fraction $f_{\text{cgm}}^{\text{sample}} = 0.14^{+0.07}_{-0.06}$ of cosmic baryons reside inside the CGM of the $10 \lesssim \log_{10}(M_{\text{halo}}/M_{\odot}) \lesssim 13.1$ halos.

We present a validation of the accuracy of our inference procedure based on mock FRB experiments in Appendix A, to which we refer the interested reader.

5. Discussion

In what follows, we examine how the results of the inference depend on the assumed choice of priors, and discuss our findings in a broader context of previous extragalactic B_{\parallel} measurements.

5.1. Effect of the IGM baryon fraction

In our analysis, we explicitly assume that IGM contribution to the RM_{obs} is negligible and do not consider f_{igm} as a free parameter in our model (see discussion in Section 3.2). Nevertheless, we need to adopt some value of f_{igm} as part of the prior for our inference algorithm. However, there is a certain degree of degeneracy between f_{igm} and f_{gas} , set by the $f_d(z)$ prior (see eq. 11), with the uncertainty due to the fact that the exact partition of the cosmic baryons between the diffuse gas in the IGM and the ionized CGM remains uncertain. Recent FRB studies have produced a mild 1σ tension in the inferred f_{igm} fractions. Khrykin et al. (2024b) have presented the first results of the FLIMFLAM survey, which utilizes a density reconstruction algorithm to constrain the LSS distribution in the foreground of 8 localized FRBs. Their analysis yielded $f_{\text{igm}} = 0.59 \pm 0.10$, mildly disfavouring strong AGN feedback (Khrykin et al. 2024a). On the other hand, Connor et al. (2025) calibrated the observed DM distribution of 69 localized FRBs (but without information on the foreground halos) to the TNG 300 hydrodynamical simulations. They found $f_{\text{igm}} = 0.76^{+0.10}_{-0.11}$ (see also Hussaini et al. 2025), pointing to a stronger feedback. In general, this discrepancy in the inferred f_{igm} values might affect the accuracy of our inference (i.e., a systematic effect). In order to quantify the significance of the f_{igm} constraint on the inference results, we repeat our MCMC analysis described in Section 4, but with different values of the mean f_{igm} fraction adopted in the $f_d(z)$ prior (see Section 4.2). The resulting 1D marginalized posterior distributions of the model parameters Θ are illustrated in Figure 6, where we show inference results for adopted $\langle f_{\text{igm}} \rangle = 0.6$ (blue), $\langle f_{\text{igm}} \rangle = 0.8$ (orange), and the intermediate case $\langle f_{\text{igm}} \rangle = 0.7$ (green). In addition, we also show the MCMC results without $f_d(z)$ prior (red curves).

It is apparent from Figure 6, that the choice of $\langle f_{\text{igm}} \rangle$ value significantly affects the resulting constraints on f_{gas} . Indeed, for $\langle f_{\text{igm}} \rangle = 0.8$, we estimate $f_{\text{gas}} \lesssim 0.22$ ($f_{\text{cgm}}^{\text{sample}} \lesssim 0.07$), which is at least $\simeq 2$ times lower than in our fiducial case with $\langle f_{\text{igm}} \rangle = 0.6$, i.e., $f_{\text{gas}} = 0.45^{+0.21}_{-0.19}$. This behaviour is expected given the functional form of the $f_d(z)$ prior described in eq. (11), in which

f_{igm} and f_{gas} are approximately complements of each other. Interestingly, the choice of $\langle f_{\text{igm}} \rangle$ does not substantially change the constraints on the $B_{\text{f/g}}^{\text{halo}}$ and $B_{\text{host}}^{\text{halo}}$, which is illustrated in the middle panels of Figure 6. Both of these quantities are linearly correlated with f_{gas} , given by eq. (6) and eq. (8). Nevertheless, we observe that even considering large changes in $\langle f_{\text{igm}} \rangle$ and the correspondingly inferred f_{gas} , imply inferences for $B_{\text{f/g}}^{\text{halo}}$ between $B_{\text{f/g}}^{\text{halo}} \lesssim 4.31 \mu\text{G}$ ($\langle f_{\text{igm}} \rangle = 0.6$) and $B_{\text{f/g}}^{\text{halo}} \lesssim 4.87 \mu\text{G}$ ($\langle f_{\text{igm}} \rangle = 0.8$), and that $B_{\text{host}}^{\text{halo}}$ and $B_{\text{host}}^{\text{local}}$ remain mostly unaffected. This is expected given that the magnetic field associated with the ISM of the host galaxy or FRB progenitor does not depend on the diffuse cosmic baryons (see eq. 9).

According to the results illustrated in Figure 6, improving constraints on f_{igm} will be crucial for obtaining the precise measurement on f_{gas} , and therefore constrain the galactic feedback models (Ayromlou et al. 2023; Khrykin et al. 2024a; Medlock et al. 2024; Connor et al. 2025; Leung et al. 2025). The upcoming FLIMFLAM DR2 (Simha et al. in prep) will incorporate analysis of ≈ 25 localized FRBs with mapping of the foreground structures, which should be enough to bring the uncertainty on f_{igm} to the $\approx 5\%$ level. Additionally, we note that throughout this work we have adopted a single f_{gas} parameter to describe the cosmic baryon fraction in all individual halos within a mass range $10 \lesssim \log_{10}(M_{\text{halo}}/M_{\odot}) \lesssim 13.1$, that our data constrains. However, hydrodynamical simulations indicate that f_{gas} is not only sensitive to the feedback prescriptions, but is also a function of the halo mass (Khrykin et al. 2024a). The FLIMFLAM-like inference would require $N_{\text{FRB}} \approx 300$ to distinguish between the f_{gas} fractions in different halo mass bins on a $\approx 10\%$ level (Huang et al. 2025). The analysis presented in this work suggests that utilizing the RM-information alone or in conjunction with FRB DMs and the LSS density reconstructions can dramatically reduce the number of FRBs required to make similar precision predictions on the f_{gas} parameter as a function of halo mass. We will explore this in future work.

In addition, a recent analysis by Zhang et al. (2025) provides an independent estimate of the cosmic baryon fraction in the CGM using the CROCODILE cosmological simulation (Oku & Nagamine 2024) with varying feedback models. They evaluate f_{igm} and f_{cgm} through two complementary approaches. First, by directly measuring the CGM mass within halos in their fiducial run, adopting $r_{\text{max}} = 1 r_{200}$ and a halo mass range of $10.5 \lesssim \log_{10}(M_{\text{halo}}/M_{\odot}) \lesssim 15.5$, they report $f_{\text{cgm}} \approx 0.11\text{--}0.16$ at $z \approx 0.28$. This total can be decomposed into $f_{\text{cgm}} \approx 0.07\text{--}0.08$ from halos with $\log_{10}(M_{\text{halo}}/M_{\odot}) = [10.5, 13.1]$ and $f_{\text{cgm}} \approx 0.09$ from halos with $\log_{10}(M_{\text{halo}}/M_{\odot}) = [13.1, 15.5]$, corresponding in our notation to $f_{\text{cgm}}^{\text{sample}} \approx 0.07\text{--}0.08$ and $f_{\text{cgm}}^{\text{other}} \approx 0.09$. Notably, despite their lower number density, the more massive halos contribute disproportionately to f_{cgm} owing to their larger gas reservoirs. Second, they derive a semi-analytic estimate of the statistically averaged intersection fraction using projected density profiles from the simulations. Applying their eq. (24), yields $f_{\text{cgm}}^{\text{sample}} \approx 0.06\text{--}0.09$ from halos with $\log_{10}(M_{\text{halo}}/M_{\odot}) = [10.5, 13.1]$, and again $f_{\text{cgm}}^{\text{other}} \approx 0.07\text{--}0.08$ in halos with $\log_{10}(M_{\text{halo}}/M_{\odot}) = [13.1, 15.5]$.

These simulation-based values are somewhat smaller than, though consistent within uncertainties, with our fiducial inference of $f_{\text{cgm}}^{\text{sample}} = 0.14^{+0.07}_{-0.06}$ for $10 \lesssim \log_{10}(M_{\text{halo}}/M_{\odot}) \lesssim 13.1$ at $\langle z \rangle \approx 0.27$. (see Section 4.3). This correspondence between two independent approaches — one with forward modelling of RM using foreground halo catalogues, and the other direct integration of simulation density profiles — provides a valuable

cross-check and highlights the utility of such comparisons for constraining feedback models in the future.

5.2. Magnetic fields in galactic environments at $0.1 \lesssim z \lesssim 1.0$

From our study of 14 FRBs, we found the average strength of the total magnetic fields in the CGM and ISM/FRB progenitor is $B \lesssim 6.5 \mu\text{G}$. In what follows, we want to place these estimate in the context of previous extragalactic measurements in the late-time Universe. To do this, we convert our results to the measurements of the B_{\parallel} by drawing samples from the MCMC marginalized posterior PDFs and randomly choosing the orientation angle of the magnetic field vectors from the corresponding uniform distributions

$$\begin{aligned} B_{\parallel,i} &= B_i \cos \alpha_i, \\ B_i &= \{B_{i,1}, \dots, B_{i,N}\} \sim p_{\text{mcmc}}(\Theta | \text{RM}_{\text{obs}}), \\ \alpha_i &= \{\alpha_{i,1}, \dots, \alpha_{i,N}\} \stackrel{i.i.d.}{\sim} \mathcal{U}[0, \pi], \end{aligned} \quad (14)$$

where i index denotes a given environment probed by our sample (i.e., foreground halos, halos and local ISM environment of the FRB hosts). Applying eq. (14) to the MCMC chains yields ≈ 4000 realizations of B_{\parallel} for each of the magnetic fields we consider in this work. We estimate $B_{\text{host},\parallel}^{\text{local}} = 3.78^{+1.70}_{-2.47} \mu\text{G}$, $B_{\text{host},\parallel}^{\text{halo}} \lesssim 3.66 \mu\text{G}$, and $B_{\text{f/g},\parallel}^{\text{halo}} \lesssim 3.12 \mu\text{G}$, respectively. Because our inference yielded constraints on the magnetic field strength associated both with the CGM of galaxies, and the ISM (and/or FRB progenitors), we compare our results separately with the results of the previous works based on a variety of techniques.

The majority of the CGM constraints come from the analysis of polarization measurements towards high- z quasars that present strong intervening Mg II absorbers (associated with galactic halos; e.g. Bernet et al. 2008; Farnes et al. 2014; Malik et al. 2020; Burman et al. 2024). Another approach is to correlate the observed RM_{obs} with the distribution of the foreground galaxies (e.g. Lan & Prochaska 2020; Heesen et al. 2023). An alternative method to estimate the B_{\parallel} is to use FRB sightlines that happen to pass through the individual known foreground halos (pioneered by Prochaska et al. 2019) or via lensing of a source's polarized emission in the ISM/halo of a foreground galaxy (Mao et al. 2017; Kovacs et al. 2025). Figure 7 presents a compilation of these measurements. It is apparent from the left panel of Figure 7, that our measurements are in good agreement with the previous estimates. We note that Prochaska et al. (2019) reported an upper limit which is marginally consistent with our measurement. Moreover, we conclude that foreground or FRB host halos might contribute (on average) a non-negligible amount of RM (thus far usually neglected), and must be taken into account when analysing future observed RM_{obs} of the FRBs.

In the right panel of Figure 7 we compare our $B_{\text{host}}^{\text{local}}$ estimate to the previous constraints on the magnetic field in the ISM of FRB hosts (Mannings et al. 2023; Sherman et al. 2023) and galaxy disks (Mao et al. 2017). The gray circles show the results obtain by Mannings et al. (2023) from the analysis of 8 FRB sightlines. Similarly, the orange circles show the B_{\parallel} measurements from the subsample of 9 DSA-110 FRBs from Sherman et al. (2023). In addition to plotting the individual measurements, we also calculate and report the average B_{\parallel} and a corresponding uncertainty for these two samples, we illustrate the resulting quantities by the gray and orange triangle markers. When calculating the average of the Mannings et al. (2023) sample, we excluded the B_{\parallel} estimate for FRB 20121102A ($|B_{\parallel}| \approx 777 \pm 366 \mu\text{G}$)

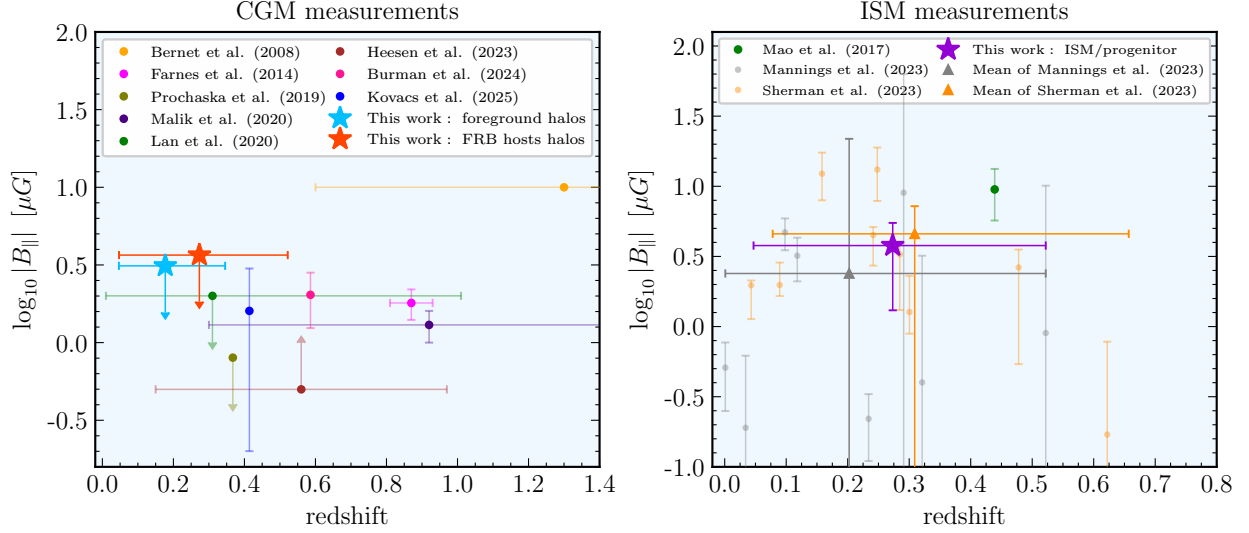


Fig. 7. Comparison of the B_{\parallel} measurements in the CGM halos obtained (left panel) and in the galactic ISM (right panel), in this (star symbols) and various previous (circles) works. We place $B_{\text{host}}^{\text{halo}}$ and $B_{\text{host}}^{\text{local}}$ estimates at the average redshift of the analysed FRB sample (see Table 1), whereas the $B_{\text{f/g}}^{\text{halo}}$ is placed at the mean redshift of the sample of foreground halos. The horizontal errorbars represent the redshift ranges of the corresponding samples.

as a clear outlier, most likely dominated by the immediate environment to the FRB. The average redshift values of Mannings et al. (2023) and Sherman et al. (2023) samples are $\langle z \rangle = 0.2023$ and $\langle z \rangle = 0.2739$, respectively; whereas ours is $\langle z \rangle = 0.2732$. We, therefore, artificially shifted the corresponding orange triangle by $\Delta z = 0.035$ in the figure, for the sake of clarity. Finally, we also show the results of the RM analysis of the individual lensed galaxy from Mao et al. (2017). Upon inspection of the right panel of Figure 7, it is apparent that we find B_{\parallel} values comparable with the average estimates from previous works. We note, however, that both of the previous works that analysed the FRB RMs did not have information about the foreground halos and attributed all the $\text{RM}_{\text{e.g.}}$ to the contribution from the local environment in the FRB host galaxies. The fact that $B_{\text{f/g}}^{\text{halo}}$, $B_{\text{host}}^{\text{halo}}$ and $B_{\text{host}}^{\text{local}}$ are all of the same order of magnitude implies that all these component must be taken into account in the RM_{obs} .

We remind the reader that our inferences are by construction average B (or average B_{\parallel}), and thus deviations from these are expected for individual cases. Based on this reasoning, a possible explanation for the apparent peak in B_{\parallel} at $z \sim 0.2$ (see Figure 1) seen in the combined samples of Mannings et al. (2023) and Sherman et al. (2023) could be most likely attributed to individual excesses of $B_{\text{host}}^{\text{local}}$ rather than $B_{\text{host}}^{\text{halo}}$ given the much larger density variations are expected (due to geometrical effects). Moreover, within the $B_{\text{host}}^{\text{local}}$ contributions of the ISM and/or local environment of the FRBs, we deem the latter to be the most likely responsible for outliers (including the possible peak at $z \sim 0.2$). This hypothesis can be tested with analysis of magnetic fields from larger samples of FRBs. Additional constraints on $B_{\text{host}}^{\text{local}}$ will also be paramount for establishing the origin of the FRB phenomenon.

6. Conclusions

We have analysed a sample of rotation measures (RM) from $N_{\text{frb}} = 14$ FRBs in the $0.05 \leq z_{\text{frb}} \leq 0.5$ redshift range, and correlated it with spectroscopic information about the foreground galactic halos, intersected by the FRB sightlines. We have devel-

oped a novel Bayesian inference formalism that allows inferring the total strength of the magnetic fields present in various galactic environments, traversed by the FRB sightlines. The main results of our work are summarized as follows:

1. For the first time, we successfully disentangle and measure the magnetic field both in the halos and ISM/progenitor environment of the FRB host galaxies. Given our fiducial set of priors we estimate that, on average, the strength of the magnetic field in the FRB host ISM and/or the FRB progenitor is $B_{\text{host}}^{\text{local}} = 5.44^{+1.13}_{-0.87} \mu\text{G}$, whereas we place an upper limit on the magnetic field associated with the FRB host halos $B_{\text{host}}^{\text{halo}} \leq 4.81 \mu\text{G}$;
2. In addition, we estimate an upper limit on the magnetic field in the halos of the foreground galaxies and groups; our analysis yielded $B_{\text{f/g}}^{\text{halo}} \leq 4.31 \mu\text{G}$, comparable to the value estimated for the halos of the FRB host galaxies. We note that for a current dataset we cannot exclude the possibility of $B_{\text{f/g}}^{\text{halo}} = 0 \mu\text{G}$ or $B_{\text{host}}^{\text{halo}} = 0 \mu\text{G}$ on a 2σ level.
3. We find that our constraints are in a good agreement with previous estimates of the strength of the parallel component of the magnetic field in the CGM of galaxies, as well, as in the ISM environment. We stress that future attempts to measure the magnetic field using FRBs must consider the contribution from the foreground halos.
4. Adopting the mNFW model to describe the radial density profile of the halos of both foreground and FRB host galaxies, we estimate the average fraction of halo baryons inside the ionized CGM of individual galaxies to be $f_{\text{gas}} = 0.45^{+0.21}_{-0.19}$. This corresponds to the fraction of cosmic baryons $f_{\text{cgm}} = 0.14^{+0.07}_{-0.06}$ inside the $10.0 \leq \log_{10} (M_{\text{halo}}/M_{\odot}) \leq 13.1$ halos.
5. Our estimates on magnetic fields in the halos of foreground and FRB host galaxies, as well as in the host ISM and/or FRB progenitor environment, are largely unaffected by the average f_{igm} value adopted in the $f_{\text{d}}(z)$ prior (see Section 4.2). On the other hand, the constraint on f_{gas} is degenerate with the f_{igm} measurement (see discussion in Section 5.1).

Results of this work emphasize the significance of the spectroscopic information regarding the foreground structures traversed by the FRB for placing accurate constraints on both cosmological and astrophysical parameters. Multiplex instruments such as MUSE (Bacon et al. 2010), 4MOST (de Jong et al. 2019) and DESI (Levi et al. 2013) will play a crucial role for interpreting DM and RM information from a surging number of FRB detections owing to increasing capabilities of the ASKAP/CRAFT (Macquart et al. 2010; Shannon et al. 2025), CHIME/VLBI (Andrew et al. 2025), CHIME/FRB Outriggers (Lanman et al. 2024; CHIME/FRB Collaboration et al. 2025), and MeerKAT TRAnsients and Pulsars (MeerTrap; Sanidas et al. 2018; Rajwade et al. 2024), as well as, DSA-110 (Ravi et al. 2023) and commissioning of the DSA-2000 (Hallinan et al. 2019). These new data will allow probing and characterizing the properties of the magnetic fields in and out of galaxies up to redshift $z \sim 1$ and beyond.

Acknowledgements. We thank Joscha Jahns-Schindler and members of the Fast and Fortunate for FRB Follow-up collaboration for useful discussion and comments. I.S.K. and N.T. acknowledge support from grant ANID / FONDO ALMA 2024 / 31240053. N.T. acknowledges support by FONDECYT grant 1252229. KN acknowledges support from MEXT/JSPS KAKENHI Grant Numbers JP19H05810, JP20H00180, and JP22K21349. Kavli IPMU was established by World Premier International Research Center Initiatives (WPI), MEXT, Japan. This work was performed in part at the Center for Data-Driven Discovery, Kavli IPMU (WPI),

References

- Abbott, T. M. C., Adamów, M., Agüena, M., et al. 2021, *ApJS*, 255, 20
- Aggarwal, K., Budavári, T., Deller, A. T., et al. 2021, *ApJ*, 911, 95
- Akahori, T. & Ryu, D. 2011, *ApJ*, 738, 134
- Akahori, T., Ryu, D., & Gaensler, B. M. 2016, *ApJ*, 824, 105
- Amaral, A. D., Vernstrom, T., & Gaensler, B. M. 2021, *MNRAS*, 503, 2913
- Andrew, S., Leung, C., Li, A., et al. 2025, *ApJ*, 981, 39
- Anna-Thomas, R., Connor, L., Dai, S., et al. 2023, *Science*, 380, 599
- Ayromlou, M., Nelson, D., & Pillepich, A. 2023, *MNRAS*, 524, 5391
- Bacon, R., Accardo, M., Adjali, L., et al. 2010, in *Society of Photo-Optical Instrumentation Engineers (SPIE) Conference Series*, Vol. 7735, Ground-based and Airborne Instrumentation for Astronomy III, ed. I. S. McLean, S. K. Ramsay, & H. Takami, 773508
- Bannister, K. W., Deller, A. T., Phillips, C., et al. 2019, *Science*, 365, 565
- Beck, R. & Wielebinski, R. 2013, in *Planets, Stars and Stellar Systems. Volume 5: Galactic Structure and Stellar Populations*, ed. T. D. Oswalt & G. Gilmore, Vol. 5, 641
- Bernales-Cortes, L., Tejos, N., Prochaska, J. X., et al. 2025, *A&A*, 696, A81
- Bernet, M. L., Miniati, F., Lilly, S. J., Kronberg, P. P., & Dessauges-Zavadsky, M. 2008, *Nature*, 454, 302
- Bertone, S., Vogt, C., & Enßlin, T. 2006, *MNRAS*, 370, 319
- Bhandari, S., Sadler, E. M., Prochaska, J. X., et al. 2020, *ApJ*, 895, L37
- Boquien, M., Burgarella, D., Roehlly, Y., et al. 2019, *A&A*, 622, A103
- Burman, S., Sharma, P., Malik, S., & Singh, S. 2024, *J. Cosmology Astropart. Phys.*, 2024, 063
- Carretti, E., O’Sullivan, S. P., Vacca, V., et al. 2023, *MNRAS*, 518, 2273
- Carretti, E., Vacca, V., O’Sullivan, S. P., et al. 2022, *MNRAS*, 512, 945
- Chambers, K. C., Magnier, E. A., Metcalfe, N., et al. 2016, *arXiv e-prints*, arXiv:1612.05560
- CHIME/FRB Collaboration, Amiri, M., Andersen, B. C., et al. 2025, *arXiv e-prints*, arXiv:2504.05192
- Chiu, I., Mohr, J. J., McDonald, M., et al. 2018, *MNRAS*, 478, 3072
- Connor, L., Ravi, V., Sharma, K., et al. 2025, *Nature Astronomy* [arXiv:2409.16952]
- de Jong, R. S., Agertz, O., Berbel, A. A., et al. 2019, *The Messenger*, 175, 3
- Dong, C., Dedieu, F., Galárraga-Espinosa, D., et al. 2025, *arXiv e-prints*, arXiv:2507.16115
- Donnert, J., Dolag, K., Lesch, H., & Müller, E. 2009, *MNRAS*, 392, 1008
- Drlica-Wagner, A., Ferguson, P. S., Adamów, M., et al. 2022, *ApJS*, 261, 38
- Faber, S. M., Phillips, A. C., Kibrick, R. I., et al. 2003, in *Society of Photo-Optical Instrumentation Engineers (SPIE) Conference Series*, Vol. 4841, Instrument Design and Performance for Optical/Infrared Ground-based Telescopes, ed. M. Iye & A. F. M. Moorwood, 1657–1669
- Farnes, J. S., O’Sullivan, S. P., Corrigan, M. E., & Gaensler, B. M. 2014, *ApJ*, 795, 63
- Foreman-Mackey, D., Hogg, D. W., Lang, D., & Goodman, J. 2013, *PASP*, 125, 306
- Fortunato, J. A. S., Bacon, D. J., Hipólito-Ricaldi, W. S., & Wands, D. 2025, *J. Cosmology Astropart. Phys.*, 2025, 018
- Glowacki, M. & Lee, K.-G. 2024, *arXiv e-prints*, arXiv:2410.24072
- Gonzalez, A. H., Sivanandam, S., Zabludoff, A. I., & Zaritsky, D. 2013, *ApJ*, 778, 14
- Gordon, A. C., Fong, W.-f., Kilpatrick, C. D., et al. 2023, *ApJ*, 954, 80
- Guo, Q. & Lee, K.-G. 2025, *MNRAS*, 540, 289
- Hackstein, S., Brüggen, M., Vazza, F., Gaensler, B. M., & Heesen, V. 2019, *MNRAS*, 488, 4220
- Hallinan, G., Ravi, V., Weinreb, S., et al. 2019, in *Bulletin of the American Astronomical Society*, Vol. 51, 255
- Heesen, V., O’Sullivan, S. P., Brüggen, M., et al. 2023, *A&A*, 670, L23
- Heintz, K. E., Prochaska, J. X., Simha, S., et al. 2020, *ApJ*, 903, 152
- Huang, Y., Simha, S., Khrykin, I. S., et al. 2025, *ApJS*, 277, 64
- Hussaini, M., Connor, L., Konietzka, R. M., et al. 2025, *arXiv e-prints*, arXiv:2506.04186
- Hutschenreuter, S., Anderson, C. S., Betti, S., et al. 2022, *A&A*, 657, A43
- James, C. W., Ghosh, E. M., Prochaska, J. X., et al. 2022, *MNRAS*, 516, 4862
- Khrykin, I. S., Ata, M., Lee, K.-G., et al. 2024b, *ApJ*, 973, 151
- Khrykin, I. S., Hennawi, J. F., Worseck, G., & Davies, F. B. 2021, *MNRAS*, 505, 649
- Khrykin, I. S., Sorini, D., Lee, K.-G., & Davé, R. 2024a, *MNRAS*, 529, 537
- Kovacs, T. O., Mao, S. A., Basu, A., Ma, Y. K., & Gaensler, B. M. 2025, *arXiv e-prints*, arXiv:2507.12542
- Kovacs, T. O., Mao, S. A., Basu, A., et al. 2024, *A&A*, 690, A47
- Lan, T.-W. & Prochaska, J. X. 2020, *MNRAS*, 496, 3142
- Lanman, A. E., Andrew, S., Lazda, M., et al. 2024, *ApJ*, 168, 87
- Lee, K.-G., Ata, M., Khrykin, I. S., et al. 2022, *ApJ*, 928, 9
- Lee, K.-G., Khrykin, I. S., Simha, S., et al. 2023, *ApJ*, 954, L7
- Leung, C., Simha, S., Medlock, I., et al. 2025, *arXiv e-prints*, arXiv:2507.16816
- Levi, M., Bebek, C., Beers, T., et al. 2013, *arXiv e-prints*, arXiv:1308.0847
- Lorimer, D. R., Bailes, M., McLaughlin, M. A., Narkevic, D. J., & Crawford, F. 2007, *Science*, 318, 777
- Lyutikov, M. 2022, *ApJ*, 933, L6
- Macquart, J.-P., Bailes, M., Bhat, N. D. R., et al. 2010, *PASA*, 27, 272
- Macquart, J. P., Prochaska, J. X., McQuinn, M., et al. 2020, *Nature*, 581, 391
- Malik, S., Chand, H., & Seshadri, T. R. 2020, *ApJ*, 890, 132
- Mannings, A. G., Pakmor, R., Prochaska, J. X., et al. 2023, *ApJ*, 954, 179
- Mao, S. A., Carilli, C., Gaensler, B. M., et al. 2017, *Nature Astronomy*, 1, 621
- McClintock, T., Rozo, E., Becker, M. R., et al. 2019, *ApJ*, 872, 53
- McQuinn, M. 2014, *ApJ*, 780, L33
- Medlock, I., Nagai, D., Anglés-Alcázar, D., & Gebhardt, M. 2025, *ApJ*, 983, 46
- Medlock, I., Nagai, D., Singh, P., et al. 2024, *ApJ*, 967, 32
- Morrissey, P., Matuszewski, M., Martin, D. C., et al. 2018, *ApJ*, 864, 93
- Moster, B. P., Naab, T., & White, S. D. M. 2013, *MNRAS*, 428, 3121
- Mitchellidze, S., Domínguez-Fernández, P., Du, X., et al. 2024, *ApJ*, 977, 128
- Oku, Y. & Nagamine, K. 2024, *ApJ*, 975, 183
- Padmanabhan, H. & Loeb, A. 2023, *ApJ*, 946, L18
- Pandhi, A., Gaensler, B. M., Pleunis, Z., et al. 2025, *ApJ*, 982, 146
- Pandhi, A., Hutschenreuter, S., West, J. L., Gaensler, B. M., & Stock, A. 2022, *MNRAS*, 516, 4739
- Petroff, E., Hessels, J. W. T., & Lorimer, D. R. 2022, *A&A Rev.*, 30, 2
- Piro, A. L. & Gaensler, B. M. 2018, *ApJ*, 861, 150
- Planck Collaboration, Aghanim, N., Akrami, Y., et al. 2018, *arXiv e-prints*, arXiv:1807.06209
- Plavin, A., Paragi, Z., Marcote, B., et al. 2022, *MNRAS*, 511, 6033
- Pomakov, V. P., O’Sullivan, S. P., Brüggen, M., et al. 2022, *MNRAS*, 515, 256
- Prochaska, J. X., Macquart, J.-P., McQuinn, M., et al. 2019, *Science*, 366, 231
- Prochaska, J. X. & Zheng, Y. 2019, *MNRAS*, 485, 648
- Rajwade, K. M., Driessen, L. N., Barr, E. D., et al. 2024, *MNRAS*, 532, 3881
- Ramesh, R., Nelson, D., Heesen, V., & Brüggen, M. 2023, *MNRAS*, 526, 5483
- Ravi, V., Catha, M., Chen, G., et al. 2023, *ApJ*, 949, L3
- Rockosi, C., Stover, R., Kibrick, R., et al. 2010, in *Society of Photo-Optical Instrumentation Engineers (SPIE) Conference Series*, Vol. 7735, Ground-based and Airborne Instrumentation for Astronomy III, ed. I. S. McLean, S. K. Ramsay, & H. Takami, 77350R
- Rodrigues, L. F. S., Chamandy, L., Shukurov, A., Baugh, C. M., & Taylor, A. R. 2019, *MNRAS*, 483, 2424
- Sanidas, S., Caleb, M., Driessen, L., et al. 2018, in *Pulsar Astrophysics the Next Fifty Years*, ed. P. Weltevrede, B. B. P. Perera, L. L. Preston, & S. Sanidas, Vol. 337, 406–407
- Scott, D. R., Dial, T., Bera, A., et al. 2025, *arXiv e-prints*, arXiv:2505.17497
- Shannon, R. M., Bannister, K. W., Bera, A., et al. 2025, *PASA*, 42, e036
- Sharma, K., Krause, E., Ravi, V., et al. 2025, *ApJ*, 989, 81
- Sherman, M. B., Connor, L., Ravi, V., et al. 2023, *ApJ*, 957, L8
- Simha, S., Burchett, J. N., Prochaska, J. X., et al. 2020, *ApJ*, 901, 134
- Simha, S., Lee, K.-G., Prochaska, J. X., et al. 2023, *ApJ*, 954, 71
- Simha, S., Tejos, N., Prochaska, J. X., et al. 2021, *ApJ*, 921, 134
- Smith, G. A., Saunders, W., Bridges, T., et al. 2004, in *Society of Photo-Optical Instrumentation Engineers (SPIE) Conference Series*, Vol. 5492, Ground-based Instrumentation for Astronomy, ed. A. F. M. Moorwood & M. Iye, 410–420
- Wang, Y.-Y., Gao, S.-J., & Fan, Y.-Z. 2025, *ApJ*, 981, 9
- Zhang, Z. J., Nagamine, K., Oku, Y., et al. 2025, *arXiv e-prints*, arXiv:2503.12741

Table A.1. Inference test results for different combinations of the input true model parameters Θ .

ID	f_{gas}	$B_{\text{f/g}}^{\text{halo}}$ μG	$B_{\text{host}}^{\text{halo}}$ μG	$B_{\text{host}}^{\text{local}}$ μG	$p(\in 68\%)$	$p(\in 95\%)$
M01	0.4	2.0	3.0	6.0	75%	97%
M02	0.7	2.0	3.0	6.0	62%	97%
M03	0.4	0.0	5.0	10.0	77%	96%
M04	0.4	3.0	2.0	6.0	76%	95%

Appendix A: Inference Test on the Mock Datasets

In order to test the accuracy of our inference algorithm described in Section 4, we apply it to the mock FRB sample. In what follows, we briefly outline the algorithm to generate mock FRB samples and the inference results.

First, we randomly draw redshifts for $N = 14$ mock FRB host galaxies from the corresponding uniform distribution $\mathcal{U}[z_{\text{min}}, z_{\text{max}}]$, where the redshift range is defined to be similar to that of our dataset in Table 1). Second, for each mock FRB galaxy in the sample we assign halo masses by sampling the corresponding uniform distribution $\mathcal{U}[M_{\text{halo}}^{\text{min}}, M_{\text{halo}}^{\text{max}}]$, where the halo mass range is given by the minimum and maximum halo masses in the dataset. Finally, for each mock FRB we create catalogues of the foreground halos. We begin by assigning the number of foreground halos per sightline. To do so we sample the uniform distribution $\mathcal{U}[N_{\text{f/g}}^{\text{min}}, N_{\text{f/g}}^{\text{max}}]$, where $N_{\text{f/g}}^{\text{min}}$ and $N_{\text{f/g}}^{\text{max}}$ are given by the number of foreground halos per sightline in the dataset (see Figure 2). Then, each i th foreground halo along the j th FRB sightline is assigned a redshift z_i^j , impact parameter from the FRB sightline b_i^j , and halo mass $M_{\text{halo},i}^j$

$$\begin{aligned}
 \{z^j\} &= \{z_{i=1}^j, \dots, z_{i=N_{\text{f/g}}}^j\} \stackrel{i.i.d.}{\sim} \mathcal{U}[0, z_{\text{FRB}}^j], \\
 \{b^j\} &= \{b_{i=1}^j, \dots, b_{i=N_{\text{f/g}}}^j\} \stackrel{i.i.d.}{\sim} \mathcal{U}[30, 3000] \text{ kpc}, \\
 \{M_{\text{halo}}^j\} &= \{M_{\text{halo},i=1}^j, \dots, M_{\text{halo},i=N_{\text{f/g}}}^j\} \stackrel{i.i.d.}{\sim} \mathcal{U}[10^{10}, 10^{13.1}] M_{\odot},
 \end{aligned} \tag{A.1}$$

where the boundaries of the intervals on which the uniform distributions are defined, are chosen to represent the observed dataset. We then assume a set of true model parameters $\Theta \equiv \{f_{\text{gas}} = 0.7; B_{\text{f/g}}^{\text{halo}} = 2.0 \mu\text{G}; B_{\text{host}}^{\text{halo}} = 3.0 \mu\text{G}; B_{\text{host}}^{\text{local}} = 6.0 \mu\text{G}\}$, and estimate the corresponding mock RM_{obs} given by eq. (3) for each mock FRB sightline. We also include an observational uncertainty by randomly sampling the Gaussian with $\sigma = 2 \text{ rad m}^{-2}$ and adding this error to the resulting mock RM_{obs} values.

Utilizing the catalogues of the foreground halos, and RM_{obs} of each mock FRB in the sample, we then proceed to calculate the joint likelihood of the mock sample, following the discussion in Section 4.1, and sample it with the MCMC algorithm. The resulting posterior PDFs are illustrated in Figure A.1, where the orange (blue) contours correspond to the 68% (95%) confidence intervals (CI), whereas the marginalized posterior PDFs for each of the model parameters are shown in the diagonal panels. The true values of the model parameters are illustrated by the dots in each panel of Figure A.1. Similar to the discussion in Section 4.3, if the maximum of a given 1D marginalized posterior PDF is at least four times larger than the larger of the two

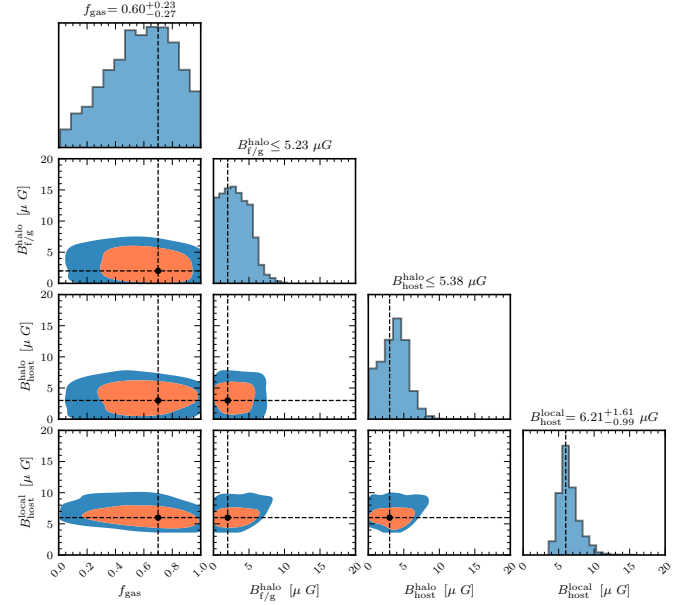


Fig. A.1. MCMC inference result for one realization of the mock sample of 14 FRBs in M02 model (see Table A.1). The red (blue) contours correspond to the inferred 68% (95%) confidence intervals. The diagonal panels show the corresponding marginalized 1D posterior probabilities of the model parameters. The black dots with dashed lines illustrate the input true values of the model parameters.

posterior PDF values at the edges of the corresponding parameter range, then we quote the 50th percentile of the marginalized posterior distributions as the measured values, while the corresponding uncertainties are estimated from the 16th and 84th percentiles, respectively. On the other hand, if the above criterion is not met, we report an upper limit by quoting the 84th percentile of the posterior PDF for a given parameter.

It is apparent from the inference results in Figure A.1, that our algorithm successfully recovers the input true values of the model parameters. However, to further verify the robustness of this result, we perform an inference test. We repeat the analysis for $N = 100$ different random realizations of the mock FRB sample, keeping Θ the same. Then, we calculate how often the true values of the model parameters fall inside the 68% and 95% CIs of the inferred posterior distributions, i.e., $p(\in 68\%)$ and $p(\in 95\%)$, respectively. For the analysis to be robust, the fraction of realizations inside each of the CI should be close to the probability level of the corresponding CI. We find $p(\in 68\%) = 62\%$ and $p(\in 95\%) = 97\%$, respectively. Therefore, because these probabilities are so close to the nominal probabilities of the corresponding CIs, we conclude that our algorithm is indeed robust. Moreover, we test different realizations of Θ as well, finding similar probability values. The results are summarized in Table A.1.